# Electron spin transport in quantum dots and point contacts

Koop, Erik Johan

# Chapter 2

# Theory, device fabrication and measurement techniques

## 2.1 Quantum Point Contacts

One of the most fundamental systems in mesoscopic physics is the Quantum Point Contact (QPC). Generally speaking a QPC is a short channel that carries ballistic one-dimensional electron transport between two reservoirs. Its conductance as a function of channel width is quantized [1, 2] and shows plateaus at integer multiples of $2e^2/h$, where $e$ is the electron charge and $h$ Planck's constant.

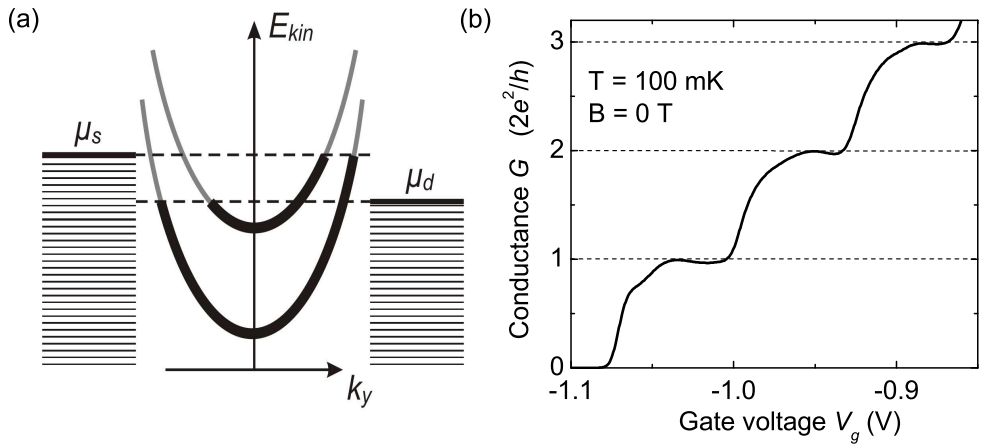


**Figure 2.1:** **(a)** Energy of one-dimensional subbands as a function of longitudinal wave function $k_y$. Electrons in the source and drain leads are filled up to their chemical potentials, $\mu_s$ and $\mu_d$. **(b)** The conductance $G$ of a QPC, quantized in steps of $2e^2/h$ as a function of gate voltage $V_g$ in zero magnetic field.

This type of device can be formed by two depletion gates on the surface of a GaAs/AlGaAs heterostructure with a 2-Dimensional Electron Gas (2DEG) below the surface. This is the so-called split gate QPC. When a negative voltage is applied to these gates with respect to the 2DEG, the 2DEG directly beneath the gates is electrostatically depleted. These constrictions can also be created by etching two trenches with a narrow gap in between. Then the 2DEG is locally destroyed. All devices presented in this thesis are formed by depletion gates.

The potential felt by the electrons near a QPC can be approximated as a saddle-point potential [3]. The confinement for the two transverse directions leads to the quantization of energy levels. There is a parabolic confinement in $x$-direction $1/2m^*\omega_0^2x^2$, like the harmonic oscillator potential, where $x$ is the direction in plane perpendicular to the current direction. In $z$-direction the confinement of the 2DEG also leads to quantization of energy levels in that direction. The energy dispersion is then

$$E_n(k_y) = \frac{h^2k_y^2}{2m^*} + E_{n,x} + E_z, \tag{2.1}$$

where $E_{n,x}$ is given by

$$E_{n,x} = (n - \frac{1}{2})\hbar\omega_0 + eV_0, \tag{2.2}$$

where $V_0$ is the bottom of the constriction, $\hbar\omega_0$ is the level separation, $k_y$ is the wave vector in $y$-direction, and $n$ labels the subbands in $x$-direction. We assume that the confinement in $z$ direction is much stronger, such that only the lowest subband in the 2DEG is occupied.

These energies describe 1-D subbands because electrons are free to move in the $y$-direction (described by the free-electron kinetic energy dispersion) but quantized in the $x$-direction. Figure 2.1 shows these 1-D subband dispersions versus the longitudinal wave vector $k_y$. Electrons in the source and drain leads fill up states in the Fermi sea to the respective chemical potentials, $\mu_s$ and $\mu_d$. The current is then determined by the number of subbands that lie below or in between these potentials.

In the next section we will derive the quantized conductance and properties of these type of devices in electric and magnetic fields. Here we will also introduce the 0.7 anomaly and other signatures of many-body effects, but we will mainly focus on non-interacting electrons. Many-body interaction effects in QPCs and their effect on the conductance properties will be discussed in more detail in Chapter 3.

## 2.2 Quantized conductance

A current will flow through the 1D conductor when a voltage $V_{sd}$ is applied across the source and the drain reservoirs. The chemical potentials of these reservoirs are then related as $eV_{sd} = \mu_s - \mu_d$ and the current that will flow is

$$I = \sum_{n=1}^{N_c} \int_0^\infty 2eN_n(E)\upsilon_n(E)[f(E,\mu_s) - f(E,\mu_d)]T_n(E)dE, \tag{2.3}$$

where $N_c = integer[\frac{E_F - eV_0}{\hbar\omega_0} + \frac{1}{2}]$ is the total number of modes propagating through the QPC, $N_n(E) = \frac{1}{2\pi}[dE_n(k_y)/dk_y]^{-1}$ is the 1D density of states, $f(E,\mu_{s,d})$ are Fermi-Dirac distributions, $T_n(E)$ is the transmission probability through the QPC and $\upsilon_n(E) = \frac{1}{\hbar}[dE_n(k_y/dk_y]$ is the group velocity. Since the product of the density of states and the group velocity in a 1D system is constant, the current is now given by

$$I = \sum_{n=1}^{N_c} \int_0^\infty \frac{2e}{h}[f(E,\mu_s) - f(E,\mu_d)]T_n(E)dE. \tag{2.4}$$

As the transport is in the linear regime (small $V_{sd}$), the difference in the Fermi-Dirac distributions is given in first order approximation as

$$f(E,\mu_s) - f(E,\mu_d) \approx -eV_{sd}\frac{\partial f(E,\mu)}{\partial E}. \tag{2.5}$$

Considering for simplicity the case of zero temperature, equation 2.4 is reduced to

$$I = \sum_{n=1}^{N_c} \frac{2e^2 V_{sd}}{h} T_n(E_F), \tag{2.6}$$

and the conductance is given by

$$G = \sum_{n=1}^{N_c} \frac{2e^2}{h} T_n(E_F). \tag{2.7}$$

If we assume unity transmission probability for each mode, $T_n = 1$, then Eq. 2.7 for the conductance reduces to

$$G = \frac{2e^2}{h} N_c. \tag{2.8}$$

Each subband contributes $2e^2/h$ to the conductance (in the absence of a magnetic field). The quantized conductance plateaus are shown in Fig. 2.1b.

Possible causes for deviations from good quantization are tunneling, scattering and reflections of electron waves in the QPC. Reflections from, or tunneling through the top of the potential barrier is visible in the experimental data as smooth transitions from one conductance plateau to another, even at zero temperature. Reflections and scattering from irregularities in the saddle point potential may lead to unwanted resonances in the conductance plateaus.

### 2.2.1 The 0.7 anomaly

The shoulder in the conductance around $0.7(2e^2/h)$ in Fig. 2.1b is the so-called 0.7 anomaly. Even though this feature was present in the first measurement of quantized conductance [1] it is still not fully understood. Nevertheless its appearance is a clear sign of the importance of many-body effects in QPCs. In Chapter 3 of this thesis we study how the appearance of the 0.7 anomaly depends on the geometry of the point contact.

One of the most striking features of the 0.7 anomaly is its temperature dependence. Figure 2.2 shows experimental results of the conductance of a QPC at different temperatures. In several detailed experimental studies [4, 5, 6, 7] it was shown that the 0.7 anomaly becomes more pronounced at elevated temperatures. When the temperature is increased, the conductance plateaus at integer multiples of $2e^2/h$ become thermally smeared. The conductance at the shoulder on the left of the $2e^2/h$ plateau, however, reduces with increasing temperature, strengthening the appearance of the 0.7 anomaly. At $T = 4.2$ K the 0.7 anomaly is the only remaining feature in the conductance.

The 0.7 feature appears and has been investigated in many other device structures, like QPCs defined in two-dimensional hole systems [8] as well as in local-oxidation-defined QPCs [9]. Several models have been proposed that relate the 0.7 anomaly to a spontaneous spin splitting in zero magnetic field [10, 11], since the 0.7 plateau evolves continuously into the spin-resolved plateau at $0.5(2e^2/h)$ when an in-plane magnetic field is applied.

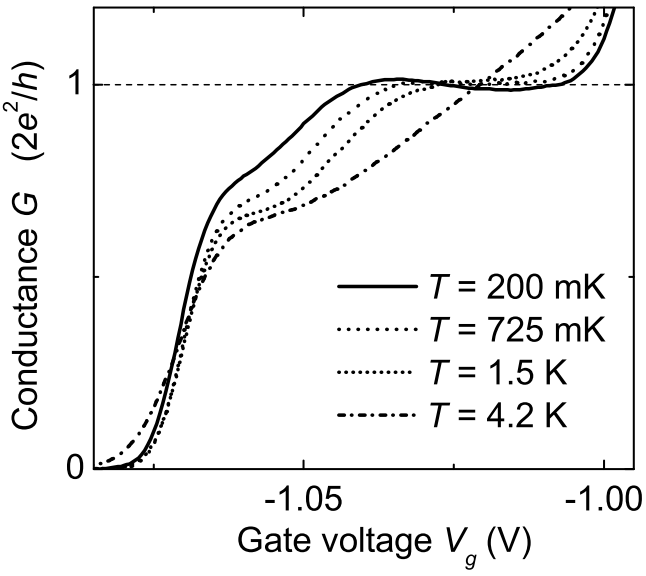


**Figure 2.2:** Conductance $G$ of a QPC as a function of gate voltage $V_g$, shown for four different temperatures. With increasing temperature the shoulder on the conductance around $0.7(2e^2/h)$ becomes more pronounced.

### 2.2.2 External magnetic fields and non-linear transport

In a non-interacting electron picture, the application of a large magnetic field splits the spin degenerate 1-D subbands by the Zeeman energy, $\Delta E_z = g^*\mu_B B$, where $g^*$ is the effective g-factor. The spin-resolved subbands each carry a conductance of $e^2/h$ as is shown in Fig. 2.3. The magnetic field considered here is applied parallel with the plane of the 2DEG.

Figure 2.4a shows the differential conductance $G = \mathrm{d}I/\mathrm{d}V$ as a function of dc source-drain bias voltage, $V_{sd}$, at many different gate voltages, $V_g$. Each line is a measurement at a different $V_g$ value. The plateaus in conductance appear as regions where many lines accumulate. In a large magnetic field of 9 T the spin-resolved plateaus are visible at multiples of $e^2/h$ (Fig. 2.4b). At high bias the so-called half-plateaus appear in the differential conductance, when the number of transport modes available for left-going and right-going electrons differs by one, i.e. when the bottom of a subband dispersion (as shown in Fig. 2.1a) lies in between the chemical potentials of the reservoirs, $\mu_s$ and $\mu_d$.

In these experiments we observe two features that are associated with many-body interactions but not fully understood. In Fig. 2.4a, the conductance peak around $V_{sd} \sim 0$ for $G < 2e^2/h$ is the zero-bias anomaly (ZBA). This peak is only

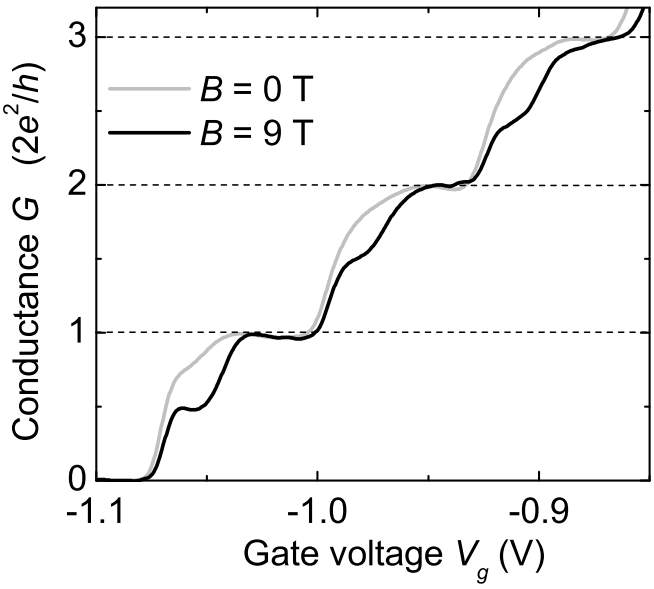


**Figure 2.3:** Conductance $G$ of a QPC as a function of gate voltage $V_g$, shown for zero and high magnetic field. Additional plateaus appear at odd multiples of $e^2/h$ in high magnetic field due to the Zeeman splitting of spin-degenerate subbands.

present at low magnetic fields and low temperatures. In the same figure, the plateaus at $0.8(2e^2/h)$ at high bias ($V_{sd} \sim \pm 1$ mV in the $B = 0$ data are also not expected in a non-interacting picture.

Figures 2.4c,d present the transconductance $\mathrm{d}G/\mathrm{d}V_g$ as a function of $V_{sd}$ for 0 T and 9 T respectively. Transitions between plateaus appear in white whereas the black regions correspond to plateaus. The central diamond shapes in the plot in zero field (labeled in units of $2e^2/h$) and the high-bias half-plateaus can be understood from a non-interacting picture. A clear explanation of this plot with corresponding energy diagrams can be found in chapter 6 of Ref. [12]. The additional lines that appear near the bottom edge of the first integer plateau are again related to the 0.7 anomaly and cannot be explained in this non-interacting model. The data in high magnetic field shows the spin-resolved plateaus. These appear as small diamonds in between the larger diamonds that are labeled in units of $2e^2/h$.

This type of experiment is in particular useful to extract information about the energy splittings between the 1-D subbands (see also Ref. [12]) and to find a lever arm for converting gate voltage $V_g$ scale into energy scale as described in Chapter 3 of this thesis.

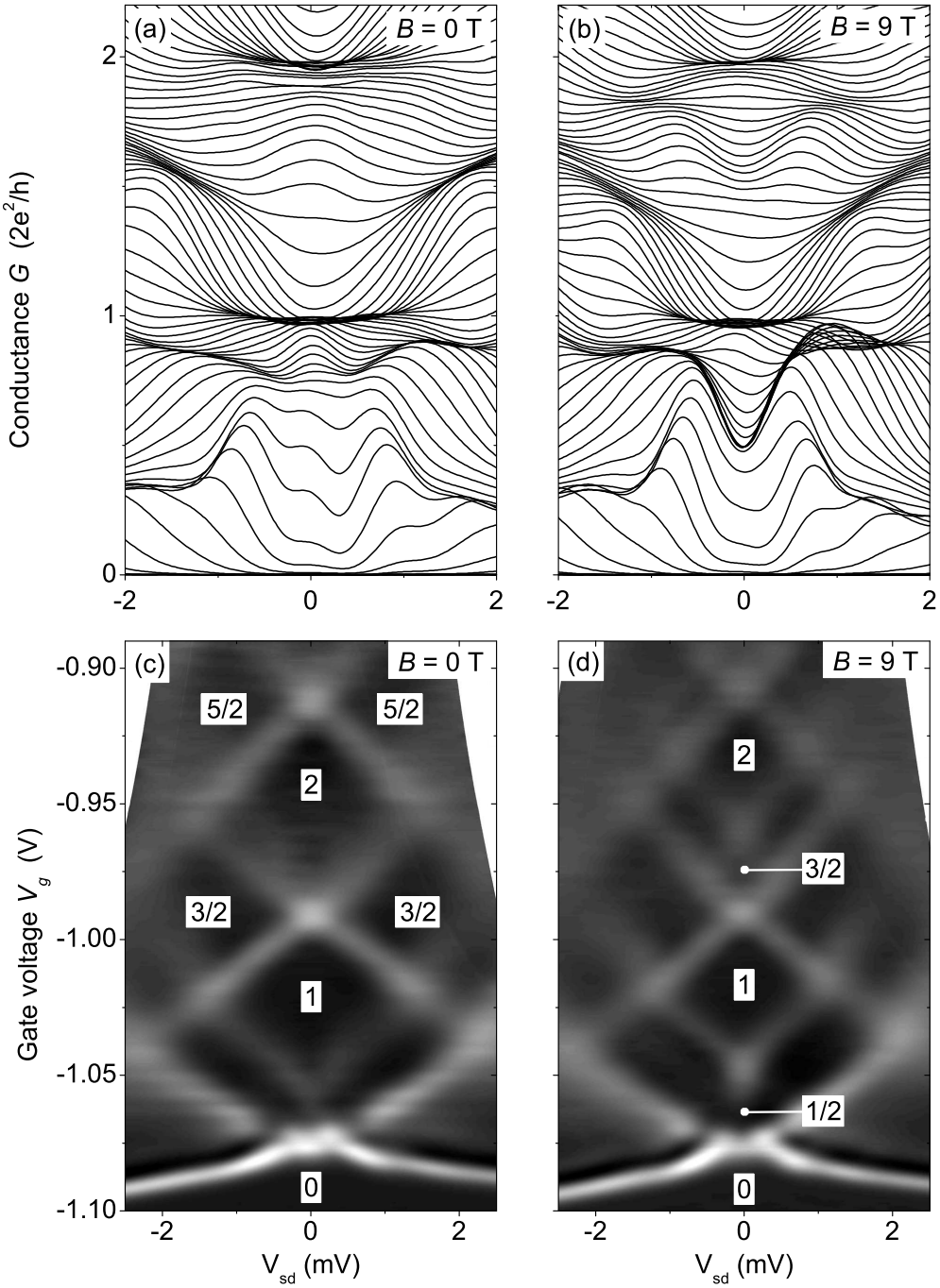


**Figure 2.4:** **(a)**, **(b)** Differential conductance $G$ as a function of DC source-drain voltage $V_{sd}$ for many different values of gate voltage $V_g$, shown for zero **(a)** and high magnetic field **(b)**. Plateaus appear as regions where many lines converge. **(c)**, **(d)** Derivative of the conductance with respect to gate voltage $\mathrm{d}G/\mathrm{d}V_g$ as a function of $V_{sd}$ for many different values of gate voltage $V_g$, shown for zero **(c)** and high magnetic fields **(d)**. White lines indicate transitions between plateaus (black regions). The conductance plateaus are labelled in units of $2e^2/h$.

## 2.3 Quantum Dots

A Quantum Dot (QD) is a device where electrons are confined in all three directions and can contain any number from a single electron to thousands of electrons [13]. For the QDs in this thesis the confinement is realized using electrostatic depletion gates. Quantum Point Contacts (QPCs) are used as tunable contacts to the dot, connecting the dot to large 2DEG reservoirs. These enable electrical transport measurements on the dot.

The coupling to these reservoirs can be in the tunneling regime, where $G_{QPC} \ll 2e^2/h$, such that the dot is very weakly coupled to the reservoirs. On the other hand, the QPCs can also be tuned to carry one or more modes of conductance, $G \sim 2e^2/h$, such that electrons can enter and exit the dot without tunneling. Measurements in these regimes are often referred to as closed dot or open dot experiments respectively.

The number of electrons in the dot can simply be changed by changing the area within the lithographically defined depletion gates. The dots we are studying are so-called large QDs and contain up to thousands of electrons. These dots are however still sufficiently small to be in the ballistic regime, where edge scattering (scattering on the walls of the QD) is much more frequent than impurity scattering.

In practice, transport in large open QDs always shows mesoscopic fluctuations of the conductance, a characteristic that results from the interference of multiple transport paths through the sample [14, 15]. Any change in the QD system which affects the accumulation of the trajectory phase, such as a small change to the the shape with a gate voltage, or by changing the accumulated (Aharonov-Bohm) phase with a perpendicular magnetic field, will alter the interference pattern, resulting in random but repeatable conductance fluctuations as a a function of the external parameter. If you want to study average properties of our system, this requires that for each measurement we need to average over sufficient statistically independent samples.

Another important effect in this type of device is Weak Localization (WL). This is an interference effect of electron trajectories scattering back to their point of origin. When Time Reversal Symmetry (TRS) is not broken and coherence is not lost, the phase accumulated along these trajectories is exactly the same as the phase of the time reversed trajectories. This creates constructive interference, leading to an increased probability for the electron to remain at the origin, hence decreasing the conductance. If TRS is broken due to for instance a strong Spin-

Orbit (SO) field, the constructive interference can be suppressed or turned into destructive interference leading to a peak in conductance. This effect is called Weak Anti-Localization (WAL). These effects can and have been used to study the coherence time in open QDs [16, 17] and SO interaction in open QDs [18] and large area 2DEG systems [19]. In our type of experiment we are typically in the regime where TRS is broken, since in practice we always suppress WL when we apply a large in-plane magnetic field, due to a small perpendicular component of that magnetic field.

For measurement on large open QDs Coulomb Blockade (CB) effects are less important because the charging energy for electrons $E_c$ decreases with increasing dot area $A$ and can be much smaller than temperature. Further the level broadening $\Gamma$ due to electrons entering and leaving the dot through the point contacts is larger than the spin degenerate mean level spacing $\Delta_m$ even for only a few modes in each point contact.

## 2.4 Device fabrication

### 2.4.1 GaAs/AlGaAs heterostructures

Fabrication of lateral structures like QPCs and quantum dots starts with a semiconductor heterostructure as shown in Fig. 2.5a. The stacked layers of GaAs and AlGaAs layers are grown by Molecular Beam Epitaxy (MBE). Dopants can be implanted during the growth process.

A 2-Dimensional Electron Gas (2DEG) forms by doping the n-AlGaAs layer with Si. The doping introduces free electrons that accumulate at the interface between the GaAs and the AlGaAs since there is a dip in the conduction band (see Fig. 2.5c). Due to the confinement in the z-direction, the energy levels in this triangular potential are quantized. The 2DEG is separated from the n-AlGaAs donor layer by an undoped AlGaAs buffer layer. This separation greatly reduces the scattering with the Si donors resulting in extremely high mobilities of the electrons in the 2DEG. Usually, the heterostructure is engineered such that only the first subband is occupied.

Figure 2.5b shows the effect of electrostatic gates on the electron gas below. This gating effect is typically realized by applying negative voltages to metal gates on top of the heterostructure.

We use heterostructures grown in the group of D. Reuter and A.D. Wieck at the Ruhr-Universität in Bochum, Germany. The sequence of the grown layers is

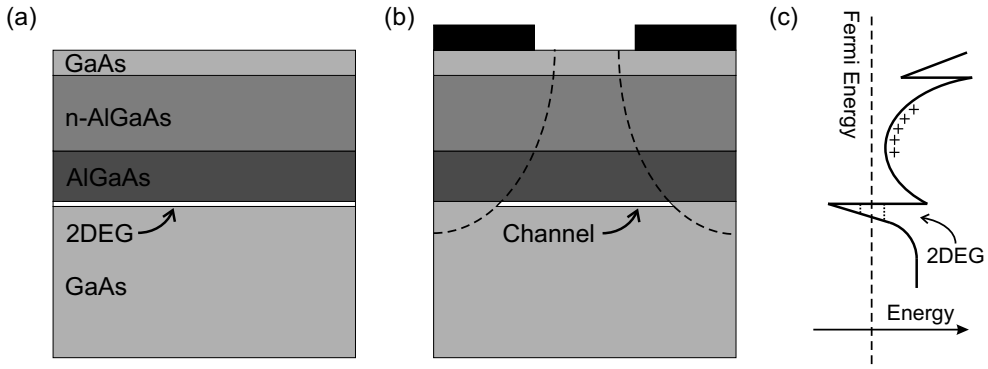


**Figure 2.5:** **(a)** Semiconductor heterostructure containing a 2DEG. **(b)** Electrons can be confined by applying negative voltages to gates on top of the wafer surface. The underlying 2DEG can then be fully depleted. **(c)** Energy band diagram for the conduction band of the heterostructure.

indicated in Fig. 2.5a. For most of the results presented in this thesis we used a heterostructure where the 2DEG is at 114 nm below the surface from modulation doping with Si. The buffer layer had a thickness of 36.8 nm and Si doping was about $n_{Si} \approx 1 \cdot 10^{24}$ m$^{-3}$. At 4.2 K, the mobility of the 2DEG was $\mu = 159$ m$^2$/Vs, and the electron density $n_s = (1.5 \pm 0.1) \cdot 10^{15}$ m$^{-2}$. In Chapters 6 and 7 we also present results where we have used another heterostructure from this group and a wafer purchased from Sumitomo Electric Industries, Inc. The specifications for all wafers can be found in Appendix A.

### 2.4.2 Electron beam lithography

The most important tool for fabrication of the devices presented in this thesis is Electron Beam Lithography (EBL). In essence it is the irradiation of a layer of an electron-sensitive polymer with a focused electron beam. The e-beam breaks the polymer chains in the resist and the exposed resist can then be selectively removed with a suitable solvent. The main advantages of EBL are high resolution and great flexibility. This general principle of EBL is depicted in Fig. 2.6.

The first EBL machines were developed in the late 1960s. Shortly thereafter it was found that polymethyl methacrylate (PMMA) made an excellent e-beam resist [20]. The resist layer that has to be used in the EBL process depends mainly on the thickness of the structure that is fabricated. In general, resists with a lower molecular weight are more sensitive to exposure and dissolve faster in a developer. Therefore the contrast of a resist becomes higher as the molecular weight of the

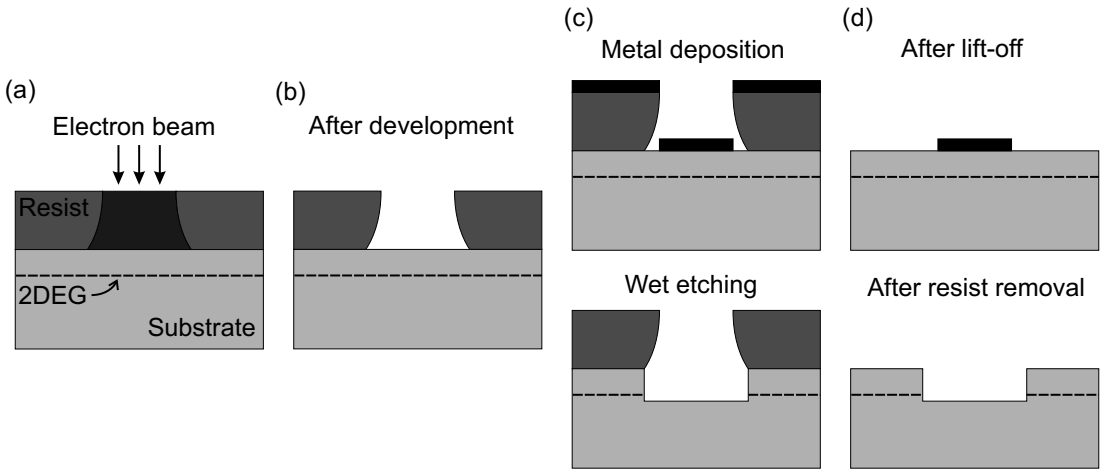


**Figure 2.6:** Electron beam lithography process to either define metal structures or to etch the surface of the heterostructure wafer. **(a)** Writing a pattern in the resist with an electron beam. **(b)** After development the exposed resist has been removed. **(c)** Evaporating metal (top figure) or wet etching (bottom figure). **(d)** After lift-off all resist, and all metal on top of that resist has been removed.

PMMA increases. To facilitate the spin coating of thin PMMA layers, the PMMA is diluted in solution.

Two different types of resist were used, 950k PMMA dissolved in chlorobenzene (2%) and 50k PMMA dissolved in ethyl-L-lactate (7%). The most common procedure is a bi-layer PMMA where the PMMA with the highest molecular weight is on top. Both layers are spin coated at 4000 rpm and then baked for 15 minutes at 170 °C. After exposure and development this results in the formation of an undercut of the bottom resist layer, which is important for a good lift-off. However for high-resolution patterns with a thickness less than $\sim$ 50 nm we use a single layer 950k PMMA resist. During ELB exposure, backscattered electrons from the substrate create an undercut even for a single layer of resist.

In our lab we use Raith E-line system for exposure. Typically we use an acceleration voltage of 10 keV, however for the high-resolution patterns we use 30 keV. The exposed polymer can be easily dissolved in a 1:3 solution of methyl-isobutyl-ketone (MIBK) and isopropanol (IPA). The developing process is stopped by rinsing in pure IPA. The unexposed resist remains unaffected. After further processing (like metal deposition or wet etching of the surface) all remaining resist and any material on top of that resist is removed using acetone. After this process, called lift-off, we rinse in IPA and spin-dry the sample.

### 2.4.3 Fabrication steps

The fabrication of devices used in this thesis required up to 5 fabrication steps. Each of these steps involves the writing of a specifically designed pattern using EBL as described in the previous section. Here we present shortly each of the steps, in Appendix B we describe the fabrication process in more detail.

#### Markers

The first fabrication step is the deposition of markers as shown in Fig. 2.7a. The marker pattern consists of 4 crosses in each corner of the device, where each line has a length of 50 $\mu m$ and a width of 5 $\mu m$. A small square is added in a specific corner of the cross for easy recognition. These markers will be used for alignment in subsequent fabrication steps. We deposit Au with a thickness of 45 nm using a Ti sticking layer.

#### Mesa

The next step is the definition of a mesa by wet etching (Fig. 2.7b). Etching the heterostructure wafer is necessary to electrically isolate conducting regions of the device. This isolation is in principle achieved when all the Si donors in the n-AlGaAs layer are removed, since they provide the electrons to form the 2DEG. In practice we always etched below the 2DEG and also removed the AlGaAs spacer layer.

The etchant is $H_2SO_4 : H_2O_2 : H_2O$, a mixture of sulphuric acid, hydrogen peroxide and DI water, with a composition 1:1:50. This results in an etching rate of approximately 2 nm/s. The etching process is stopped by rinsing the sample in DI water. Finally we spin-dry the sample.

#### Ohmic contacts

Electrical contacts to the 2DEG are realized by thermal annealing of surface electrodes in the shape of bonding pads. These electrodes have an area of 150 by 150 $\mu m^2$ and are located at specific places near the edge of the mesa (Fig. 2.7c). We make sure that the edge of the ohmic contact intersects the mesa edge at several places, such that there can be no edge currents around an ohmic contact.

We deposit 150 nm of Au and Ge in a eutectic mixture of 88:12 wt% followed by a layer of Ni with a thickness of 30 nm and a layer of Au with a thickness of 20 nm. The melting temperature of the eutectic AuGe mixture is 363 °C. For

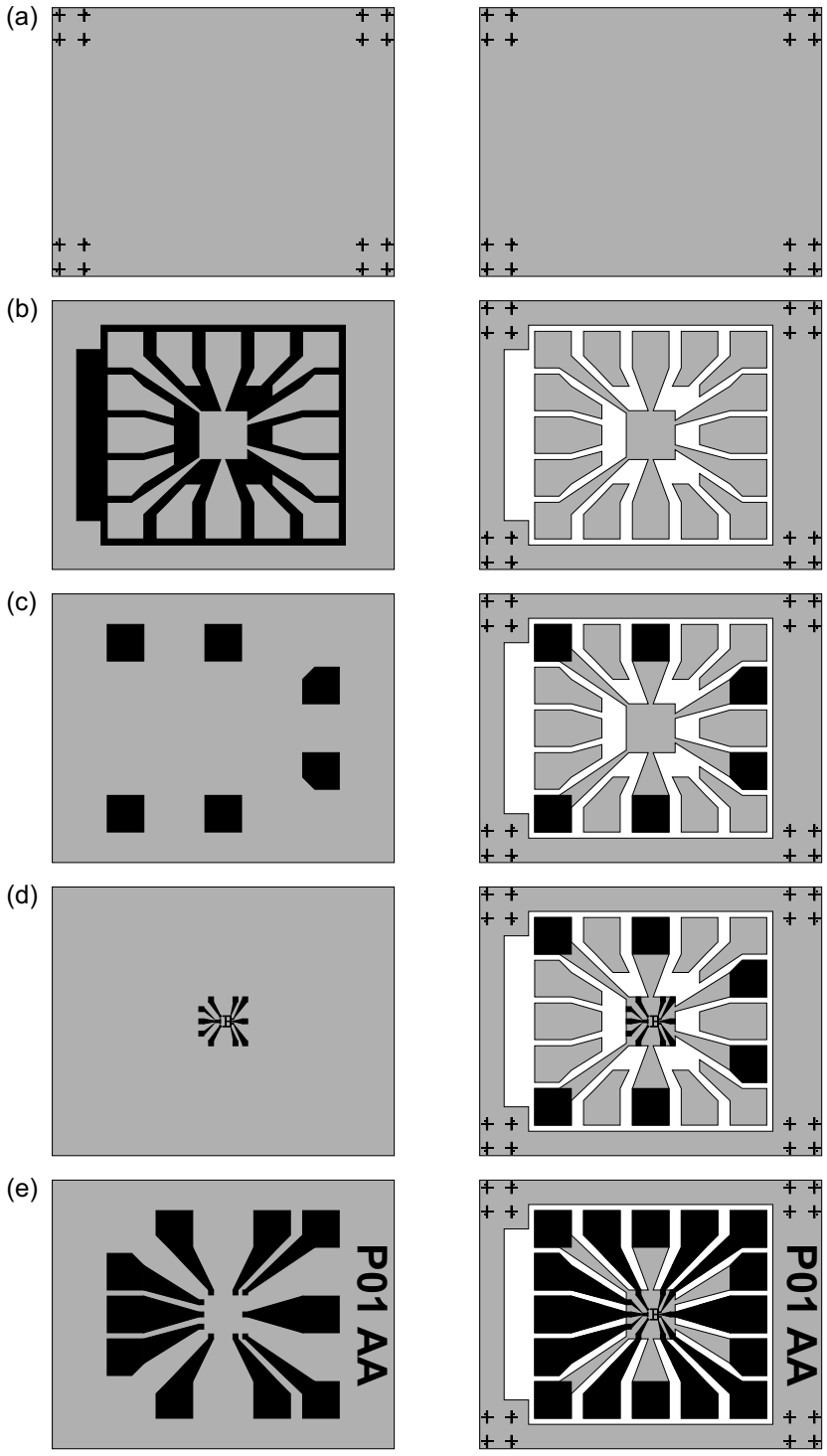


**Figure 2.7:** Electron beam lithography patterns for the fabrication of Quantum Point Contact and Quantum Dot devices. Each individual step is shown in the left image while the right image shows the sequential result for **(a)** alignment markers, **(b)** mesa etching, **(c)** ohmic contacts, **(d)** small gates (not to scale), and **(e)** large gates.

the annealing we use a quartz tube oven at 450 °C with an $N_2$ flow to prevent oxidation. Further, for devices that were accidentally annealed without an $N_2$ flow we have found that a conducting layer forms on the surface of the wafer.

During the annealing the electrodes melt and diffuse into the heterostructure wafer. The metal-rich phases penetrate into the wafer but do not actually reach the 2DEG. The Ge atoms form a highly doped region in between the diffused metal and the 2DEG, resulting in linear IV characteristics for the contact. At 4.2 K the contact resistance is typically well below 1 kΩ. The results of an in depth study on the fabrication of ohmic contacts can be found in chapter 7 of this thesis.

#### Fine gates

This step is the most critical step in the sample fabrication, since in this step the gates defining the quantum point contacts and quantum dots are made. The structures are defined in the center of the mesa as shown in Fig. 2.7d.

The pattern is written with a larger acceleration voltage for the electrons of 30 keV (compared to 10 keV for the other steps) to reduce proximity effects. We deposit 15 nm of Au with a Ti sticking layer. In this step the lift-off has to be done more carefully, typically the sample is left in heated acetone for several hours.

#### Large gates

The fabrication of the large gates is necessary to connect the fine gates to large bonding pads on the outside of the mesa (Fig. 2.7). We deposit a thick layer (typically 150 nm) of Au with a Ti sticking layer to overcome the height step of the mesa.

After the processing is finished, the sample is glued onto a chip carrier with varnish and bonding wires are attached to the bonding pads.

## 2.5 Measurement techniques

### 2.5.1 Dilution refrigerator

Our measurements are done at temperatures well below 1 K, in order to resolve very small energy differences. We use a $^3$He/$^4$He dilution refrigerator purchased from Leiden Cryogenics, which has a base temperature less than 10 mK and

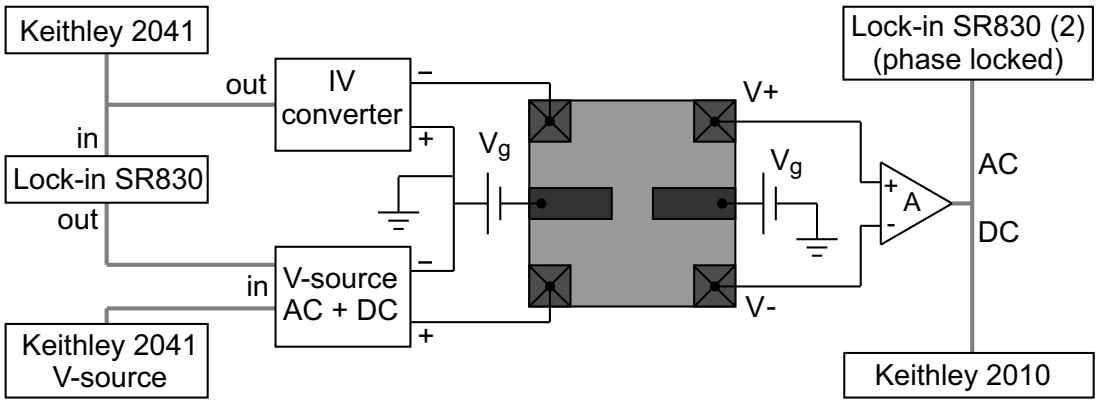


**Figure 2.8:** Circuit drawing of a 4-terminal voltage-bias measurement. Thin black wires carry very small signals at the sample level, connected to a clean ground and electrically isolated from the thick grey wires. These wires carry signals at the 1 V level that are connected to our measurement equipment.

a cooling power of about 1 mW at 100 mK. The sample is mounted onto a sample holder, thermally anchored to a cold finger, and inside a series of 3 copper cans that act as radiation shields. The sample holder is placed in the bore of a superconducting magnet that can apply a magnetic field up to 9 T.

### 2.5.2 Measurement electronics

Many properties of our devices can be studied by measuring the resistance $R = V/I$ or conductance $G = I/V$ of the device. In practice we mostly measured the differential resistance or differential conductance using a lock-in technique. There are two common measurement geometries to determine the resistance of a sample. One where a fixed current is passed through the device and the voltage drop is measured, or vice versa. This is called a current biased or voltage biased measurement respectively.

A voltage biased measurement is typically used when $R_{device} > e^2/h$, because all resistances in series with the sample add up to determine the current $I = V_{sd}/R_{total}$, where $R_{total} = R_{device} + R_{ohmics} + R_{wiring} + R_{IVconv}$. The input impedance of the IV converter $R_{IVconv} = 2$ kΩ for the most typical choice of the feedback resistance (10 MΩ). The sample resistance is ideally much larger than the other resistances in the set-up. Because in our measurements this requirement is not always met we use an additional set of voltage probes to determine the voltage drop across the device $\Delta V$. Then the resistance of the device can be

determined as $R_{device} = \Delta V/I$.

An important condition for our measurements (in the linear regime) is that the voltage drop across the device $V_{sd}$ is smaller than temperature $eV_{sd} < kT$. This can be achieved using a voltage biased measurement or by actively checking with a current biased measurement.

Here we will describe the 4-terminal voltage biased measurement as drawn in Fig. 2.8. The AC modulation voltage of an SR830 lock-in amplifier is used, if so desired together with a DC voltage from a Keithley 2041, to control the output of the voltage source. The inputs are passed through isolation amplifiers to isolate the sample electrically from the measurement electronics. An IV converter, or transimpedance amplifier, measures a voltage proportional to the current through the device. The non-inverting input (+) of the amplifier is grounded. Then its inverting input (-), although not connected to ground, will assume a similar potential, becoming a virtual ground. The AC component of the IV converter output is, after passing through an isolation amplifier, measured by the SR830 lock-in, the DC component is measured by the Keithley 2041. We typically use lock-in frequencies of 11 Hz for quantum dot measurements and 380 Hz for point contact measurements, and $V_{sd} = 10$ $\mu$V. Lower frequencies are required for the quantum dot experiments because there can be a large resistance in the voltage probe path.

The voltage difference measured by the two voltage probes on the right side of Fig. 2.8 is amplified by a factor 10 to $10^4$ and measured by a second SR830 lock-in (phase locked to the first) and a Keithley 2010 multimeter. Voltages to the gates are applied via 8 Digital-to-Analogue Converters (DACs). These DACs are floating voltage sources where we connect the ground to the minus wire of the bias voltage source.

We use LabView to control the measurements. All signals are sent to the computer via a GBIP interface. This computer also controls the DAC outputs via an optical fiber.

### 2.5.3 Measurement wires and filtering

In between measurement electronics and the device, several filtering stages are required to ensure that the effective electron temperature is close to the lattice temperature. In practice the effective electron temperature is always higher due to interference and noise.

Four sets of 12 twisted pair manganin wires (making a total of 96 wires) with

a diameter of 0.13 mm run all the way from room temperature down to base temperature. To minimize the heat load on the mixing chamber, these wires are thermally anchored near the top of the IVC at 4.2 K, at the 1K pot ($\sim$ 1.5 K), at the still ($\sim$ 500 mK), at the 80 mK plate, and finally at the mixing chamber.

At room temperature all wires are connected to a pi-filter, or capacitor-input filter. This filter acts as a low-pass filter and consists of a 1.5 nF capacitor to ground, an inductive element in series and another 1.5 nF capacitor to ground. At the mixing chamber all wires go through copper powder filters [21]. These are copper tubes in which 4 measurement wires are wound, each with a length of $\sim$ 3 m. The tubes are then filled with copper powder to create a large contact area with the wires. The resistance of these wires, in combination with their stray capacitance, RC-filters high-frequency noise.

# References

[1] B. J. van Wees *et al.*, Phys. Rev. Lett. **60**, 848 (1988).

[2] D. A. Wharam *et al.*, J. Phys. C **21**, L209 (1988).

[3] M. Büttiker, Phys. Rev. B **41**, 7906 (1990).

[4] K. J. Thomas *et al.*, Phys. Rev. Lett. **77**, 135 (1996).

[5] K. J. Thomas *et al.*, Phys. Rev. B **58**, 4846 (1998).

[6] A. Kristensen *et al.*, Phys. Rev. B **62**, 10950 (2000).

[7] S. M. Cronenwett *et al.*, Phys. Rev. Lett. **88**, 226805 (2002).

[8] R. Danneau *et al.*, Appl. Phys. Lett. **88**, 012107 (2006).

[9] L. P. Rokhinson, L. N. Pfeiffer, and K. W. West, Phys. Rev. Lett. **96**, 156602 (2006).

[10] R. Fitzgerald, Phys. Today **55**, 21 (May 2002).

[11] K. Ensslin, Nature Phys. **2**, 587 (2006).

[12] S. M. Cronenwett, Ph. D. Thesis, Stanford University (2001).

[13] L. Kouwenhoven and C.M. Marcus, Physics World **11**, 35 (1998).

[14] R. Washburn, R.A. Webb, Rep. Prog. Phys. **55**, 1311 (1992).

[15] C. M. Marcus *et al.*, Phys. Rev. Lett. **69**, 506 (1997).

[16] A.G. Huibers *et al.*, Phys. Rev. Lett. **81**, 200 (1998).

[17] A.G. Huibers *et al.*, Phys. Rev. Lett. **83**, 5090 (1999).

[18] D. M. Zumbühl *et al.*, Phys. Rev. Lett. **89**, 276803 (2002).

[19] J. B. Miller *et al.*, Phys. Rev. Lett. **90**, 76807 (2003).

[20] M. Hatzakis, J. Electrochem. Soc. **116**, 1033 (1969).

[21] J. M. Martinis, H. M. Devoret, and J. Clarke, Phys. Rev. B **35**, 4682 (1987).